Biomedical Physics & Engineering Express

PAPER

The value of using heterogeneous detector groups for the development of time-of-flight (TOF) positron emission tomography (PET) systems

Zhiqiang Xin[1], **Chien-Min Kao**[2,*], **Yuqing Liu**[3], **Xun Chen**[1], **Labao Zhang**[4], **Peiheng Wu**[4] and **Qingguo Xie**[1,3,5]

[1] Department of Electronic Engineering and Information Science, University of Science and Technology of China, Hefei 230022, People's Republic of China
[2] Department of Radiology, The University of Chicago, 5841 S. Maryland Avenue, Chicago, Illinois 60637, United States of America
[3] Institute of Artificial Intelligence, Hefei Comprehensive National Science Center, Hefei 230094, People's Republic of China
[4] Research Institute of Superconductor Electronics, School of Electronic Science and Engineering, Nanjing University, Nanjing 210093, People's Republic of China
[5] Wuhan National Laboratory for Optoelectronics, Wuhan 430074, People's Republic of China
[*] Author to whom any correspondence should be addressed.

E-mail: c-kao@uchicago.edu

Keywords: TOF PET, system design, target-region imaging, mixed time resolution

OPEN ACCESS

RECEIVED
5 May 2023

REVISED
27 July 2023

ACCEPTED FOR PUBLICATION
11 August 2023

PUBLISHED
23 August 2023

Original content from this work may be used under the terms of the Creative Commons Attribution 4.0 licence.

Any further distribution of this work must maintain attribution to the author(s) and the title of the work, journal citation and DOI.

Abstract

Objective. Much recent attention on positron emission tomography (PET) is the development of time-of-flight (TOF) systems with ever-improving coincidence time resolution (CTR). This is because, when all other factors remain the same, a better CTR leads to images of better statistics and effectively increases the sensitivity of the system. However, detector designs that aggressively improve the CTR often compromise the detection efficiency (DE) and offset the benefit gained. Under this circumstance, in developing a TOF PET system it may be beneficial to employ heterogeneous detector groups to balance the overall CTR and DE of the system. In this study, we examine the potential value of this system design strategy by considering two-dimensional systems that assume several representative ways of mixing two detector groups. *Approach*. The study is based on computer simulation and specifically considers medium time-resolution (MTR) detectors that have a 528 ps CTR and high time-resolution (HTR) detectors that have a 100 ps CTR and a DE that is 0.7 times that of the MTR detector. We examine contrast recovery, noise, and subjective quality of the resulting images under various ways of mixing the MTR and HTR detectors. *Main results*. With respect to the traditional configuration that adopts only the HTR detectors, symmetric heterogeneous configurations may offer comparable or better images while using considerably fewer HTRs. On the other hand, asymmetric heterogeneous configurations may allow the use of only a few HTRs for improving image quality locally. *Significance*. This study demonstrates the value of the proposed system-level design strategy of using heterogeneous detector groups for achieving high effective system sensitivity by factoring into the tradeoff between the CTR and DE of the detector.

1. Introduction

Time-of-flight (TOF) positron emission tomography (PET) is known to yield higher image signal-to-noise ratios (SNR) than does non-TOF PET in such a way that a higher TOF resolution, which is often given by the coincidence time resolution (CTR) in FWHM, leads to a higher image SNR gain (Lewellen 1998, Conti 2011a, 2011b). As a result, there has been substantial interest in improving the CTR (Conti 2011a, 2011b, Conti and Bendriem 2019). New technologies that have the potential to achieve 10 ps CTR are being investigated (Lecoq 2017). When the CTR reaches the image voxel size, reconstruction-free direct imaging is also possible, as the UC Davis group had recently demonstrated by using a pair of Cherenkov-radiator-integrated microchannel-plate photomultipliers that were capable of 34 ps CTR (Kwon *et al* 2021). At present, essentially all high-end clinical PET systems are TOF capable and they are based on detectors made of pixelated, fast, and bright inorganic scintillators such as lutetium(-yttrium)

© 2023 The Author(s). Published by IOP Publishing Ltd

oxyorthosilicate (L(Y)SO) whose light outputs at the end surface are read by using silicon photomultipliers. The CTRs of these systems are in the range of 300–400 ps (Miller *et al* 2015, Pan *et al* 2019), with a recent system reporting a 210 ps CTR (Van Sluis *et al* 2019). CTRs in the range of 100–200 ps were reported for various small L(Y)SO crystals (Hyman 1965, Moszynski and Bengtson 1979, Kyba *et al* 2008, Conti *et al* 2009). Generally, the CTR degrades as the crystal thickness increases. For example, Gundacker *et al* reported that in the laboratory the CTR deteriorates from 108 $\pm$ 5 ps to 176 $\pm$ 7 ps when the LSO crystal thickness increases from 3 mm to 20 mm (Gundacker *et al* 2014). On the other hand, as a smaller crystal thickness yields a lower detection efficiency (DE), L(Y)SO-based clinical systems employing detectors shorter than 20 mm may lack adequate sensitivity (Nikolopoulos *et al* 2006). For detectors capable of depth-of-interaction (DOI) measurement, one may improve the CTR of thick crystals by performing time correction based on DOI. As an example, Pizzichemi *et al* reported a 157 ps CTR for 15 mm thickness LYSO crystals (Pizzichemi *et al* 2019). The Stanford group proposed to couple compact photodetectors along a side surface of a scintillator slab to improve light collection and reduce photon transit-time jitter, achieving a CTR of about 100 ps for 20 mm thickness LGSO detectors (Cates and Levin 2018, Pourashraf *et al* 2021a, 2021b). Overall, developing practical PET detectors that have a high DE and 200 ps or better CTR remains an active ongoing research topic.

At present, as high time-resolution (HTR) detectors are likely to have compromised DEs, a PET system employing such detectors to achieve a superior TOF resolution will take place at the expense of the physical sensitivity. As a result, the effective sensitivity of the system may not be much higher than, or even can be lower than, that of a system that is based on detectors having somewhat inferior CTR but higher DE. Also, an important recent trend in PET is the development of total-body (TB) systems with an axial length exceeding one meter (Badawi *et al* 2019). A TB-PET system that is entirely based on HTR detectors can be prohibitively expensive (Vandenberghe *et al* 2020). Previously, we have examined the approach of employing a mixture of high and medium spatial-resolution detectors for developing a PET system that has a suitable overall resolution for clinical imaging while providing a boosted resolution for certain regions (Liu *et al* 2014). Motivated by this previous work, in this paper we study mixing the use of high-time-resolution (HTR) and medium-time-resolution (MTR) detectors as a system-level design strategy for addressing the issue of diminished detector DE and increased cost when improving detector CTR. So far, this issue has not received much research attention. As a proof-of-concept work, this paper considers two-dimensional (2d) imaging and conducts simulation studies in which factors other than DE that can be affected when improving CTR are ignored. It will produce data showing that, as postulated, when using HTR detectors the gain in sensitivity due to its high CTR can be lost due to its diminished DE. For examining the possibilities and limitations of the proposed strategy, we consider several configurations of mixing the HTR and MTR detectors, including symmetric and asymmetric ones, and the use of only a small number of HTR for improving the image quality in a focus area.

The remainder of this paper is organized as follows. In section 2, we describe the system configurations of interest, the generation of simulation data, the image reconstruction algorithm, and the figures of merit (FOM) for consideration in the evaluation study. Section 3 describes the numerical experiments and their results. Conclusions and discussion are given in section 4.

2. Method

2.1. System configurations

Figure 1 shows the five 2d system configurations employing two groups of detectors having different CTRs considered in this paper. Mimicking the Biograph mCT Flow Edge scanner, which is one of the first-generation modern clinical TOF PET systems (Jakoby *et al* 2011, Rausch *et al* 2015), these systems contain 48 detector modules and have a ring diameter of approximately 842 mm. Each detector module contains 13 LSO crystals that are 4 mm (transaxial) $\times$ 4 mm (axial) $\times$ 20 mm (radial) in size. The field-of-view (FOV) has a diameter of 78 cm. As shown in figure1, in the M1 configuration the MTR and HTR detectors are interleaved and evenly distributed on the detector ring. In contrast, the M2 (M3) configuration contains an MTR detector-only arc that has 24 (36) detector modules and an HTR detector-only arc that has 24 (12) detector modules. Of these configurations, we expect the M1 configuration to yield more uniform image properties. On the other hand, the M2 and M3 configurations can be easier to build. Also, they may be of interest for the development of certain organ-specific systems. The M4 and M5 configurations have only four HTR detectors. They are considered for testing whether it is possible to use a small number of HTR detectors to boost the image quality in the common region seen by them, which is called the *focus area* below.

In this paper, we chose the MTR detector to have a 528 ps CTR and the system to have a 4.06 ns coincidence time window, equal to the nominal values of the Biograph mCT Flow Edge. On the other hand, the HTR detector was assumed to have a 100 ps CTR, which has been achieved in the lab. We assume that the CTR is the quadrature sum of the time resolution of the two detectors involved in coincidence detection. Therefore, by saying the HTR and MTR detectors have

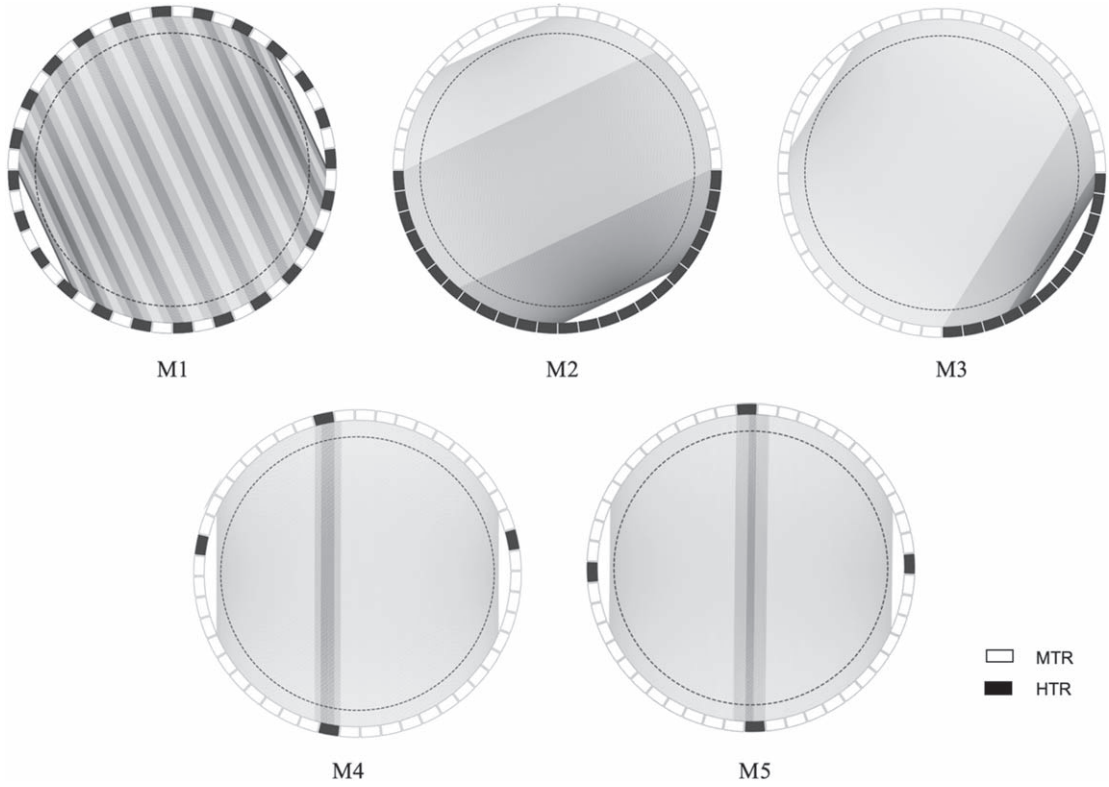

Figure 1. Five 2d system configurations that employ a mixture of HTR and MTR detectors. In the M1 configuration, the HTR detectors (marked in black on the detector ring) and MTR detectors (marked in white on the detector ring) are interleaved and evenly distributed on the detector ring. In the M2 and M3 configurations, the detector ring is made of an HTR detector-only arc and an MTR detector-only arc. The HTR detectors account for one-half (one-fourth) of the total number of detectors in M2 (M3). In the M4 and M5 configurations, the system contains only four HTR detectors to provide a certain focus area, which is the intersecting region of these detectors. In M4 (M5), the focus area is away from (at) the center of the FOV. These systems produce three types of LORs. A type-M LOR involves two MTR crystals (some such LORs are shown in light grey). A type-H LOR involves two HTR crystals (some such LORs are shown in dark grey). A type-HM LOR involves one MTR crystal and one HTR crystal (some such LORs are shown in grey). The FOV of the system is indicated by the dashed-line circle.

100 ps and 528 ps CTRs we mean that the detectors have a time resolution of 70.7 ps and 373.4 ps, respectively. The five configurations in figure1 produce three types of events or lines of response (LOR). Type-M and type-H events (LORs) are those that involve two MTR crystals and two HTR crystals respectively, while type-HM events (LORs) are those that involve one HTR crystal and one MTR crystal. Therefore, the CTRs for the type-H, type-M, and type-HM events (LORs) are 528 ps, 100 ps, and 379 ps, respectively. Per convention, time resolutions and CTRs in this paper are the FWHM values.

We also considered the traditional configurations that employ a single detector type, serving as performance references. These configurations are identified as S-*n*, where *n* is the CTR of the detector. Hence, the S-528 (S-100) configuration employs only the MTR (HTR) detectors.

2.2. Generation of simulation data

Simulation data were generated by using an in-house Python 3.7.6 program. The LORs of a system were obtained by connecting the front centers of any two crystals of the system. As explained above, there are type-M, type-H, and type-HM LORs that have different CTRs. For a given LOR *i*, Siddon's raytracing algorithm (Siddon 1985) was used to identify all image pixels that the LOR intersected with to obtain a set of image pixel values f_j, their locations on the LOR τ_{ij}, and the lengths of the LOR segments inside these pixels h_{ij}. Several TOF bins of a certain width were placed along the LOR (to be explained below). As depicted in figure2, to compute the contribution of f_j to measurement at TOF bin k, a one-dimensional Gaussian $p(t)$ whose FWHM equals the CTR of the LOR was placed along the LOR and centered at τ_{ij}. The area of $p(t)$ under TOF bin k, denoted by p_{ikj}, was numerically calculated. The noise-free measurement at TOF bin k of LOR i was then given by

$$y_{ik} = \alpha_i \sum_j p_{ikj} h_{ij} f_j \qquad (1)$$

where $\alpha_i > 0$ was introduced to allow assigning different DEs for the HTR and MTR detectors. Given a numerical phantom, noise-free measurements at all TOF bins and all LORs of the system were first computed by the above procedure and stored. Noisy measurements were then obtained by scaling the noise-free measurements to have a specified total number of counts and Poisson variates whose means

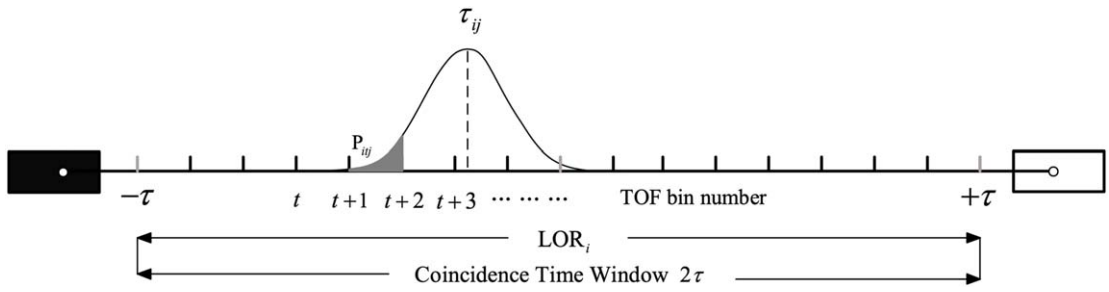

Figure 2. Computation of the TOF weight of an image pixel to a TOF bin. The standard deviation of the Gaussian kernel is determined by the CTR of the LOR. See text for detail.

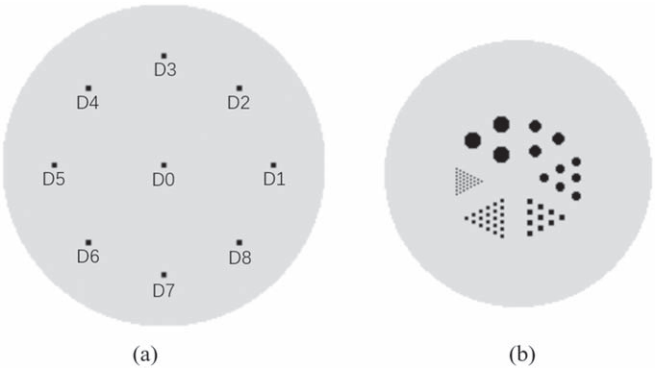

Figure 3. The two numerical phantoms considered. (a) Phantom 1 contains 9 point-like sources (6 mm diameter) on a 36 cm diameter background disc. The sources are identified as D0 to D8 as shown. (b) Phantom 2 contains six groups of sources, whose diameters are 18 mm, 14 mm, 10 mm, 6 mm, 4 mm, and 2 mm, on a 30 cm diameter background disc. The center-to-center spacing between two sources in the same group is twice the source diameter. For both phantoms, the source-to-background activity ratio is 4:1.

equal the scaled noise-free measurements were drawn. The scaling factor applied was recorded and later used to convert the reconstructed images to the intensity scale of the numerical phantom (hence, if Poisson noise is not introduced the resulting image will be identical to the phantom). Subject attenuation, blurring due to the detector size, positron range, and photon acolinearity were not modeled. Also, scattered and random events were not included.

The number of TOF bins and their widths on a LOR were determined as follows. The measurement interval on a LOR was given by the 4.06 ns coincidence time window employed, which was equivalent to a length of approximately 60.9 cm. This length was divided into an odd number of TOF bins whose width was approximately equal to one-half of the CTR value of the LOR. This results in eighty-one (81) 50 ps bins, twenty-one (21) 193 ps bins, and fifteen (15) 270 ps bins for type-H, type-HM, and type-M LORs, respectively.[6]

2.3. Image reconstruction

For image reconstruction, we employed the maximum-likelihood expectation-maximization algorithm for TOF PET (TOF-MLEM) (Conti *et al* 2005), given by

$$f_j^{(n+1)} = f_j^{(n)} \left(\frac{1}{\sum_{i,k} \alpha_i p_{ikj} h_{ij}} \right) \sum_{i,k} \frac{p_{ikj} h_{ij} g_{ik}}{\sum_l p_{ikl} h_{il} f_l^{(n)}} \quad (2)$$

where $f_j^{(n)}$ is the estimated image value at pixel j at nth iteration, g_{ik} is the measurement at TOF bin k and LOR i, and the product $\alpha_i p_{ikj} h_{ij}$ is the contribution of a unit image value at pixel j to measurement at TOF bin k of LOR i (see section 2.2). In equation (2), p_{ikj} is computed on-the-fly as described above in section 2.2 by using the CTR associated with LOR i. The LOR-specific CTR can be readily determined as the index i uniquely identifies the types of the two detectors that define the LOR and hence its event type (see section 2.1).

For all reconstructions, the initial image estimate had a unit value at all image pixels. During each iteration, α_i, h_{ij}, and p_{ikj} were obtained on the fly. One hundred and twenty (120) iterations were performed and results at all iterations were saved.

2.4. Numerical phantoms and image-quality evaluations

Figure 3 shows the two numerical phantoms employed. The first phantom, shown in figure3(a) and called *Phantom 1* below, was used for quantitative image-quality assessment. It was a circular disc of a 36

[6] To test whether this TOF bin size is adequate, we compared the CRC-versus-BV curves obtained for the M1–1/2 configuration by using this bin size and by using a finer bin size that equals one-tenth of the CTR. Essentially identical results were obtained.

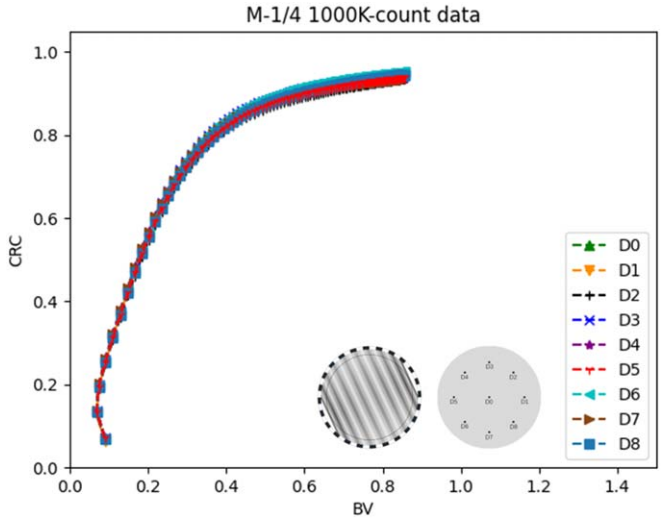

Figure 4. The CRC-versus-BV curves for the nine sources of Phantom 1 for the M1–1/4 configuration with 1,000K events. The MTR and HTR detectors have the same DE. The insert shows Phantom 1 (35 cm diameter) and the M1 configuration of the scanner (78 cm diameter). For visuality, they are not shown at the same scale.

cm diameter that contained nine (9) 6 mm-diameter sources, identified by D0 to D8 as shown. The activity ratio of the sources to the background was 4:1. The second phantom, shown in figure3(b) and called *Phantom 2* below, was a Derenzo-like phantom for visibility assessment. It had a 30 cm diameter background and six (6) groups of sources of 18 mm, 14 mm, 10 mm, 6 mm, 4 mm, and 2 mm diameters. The center-to-center spacing between two sources in the same group was equal to two times the source diameter. The source-to-background ratio was also 4:1. As with Biograph mCT Flow Edge, the numerical phantoms and all reconstructed images consisted of 400×400 2-mm square pixels.

Given a reconstructed image of Phantom 1, two FOMs were obtained, including the contrast recovery coefficient (CRC) and background variability (BV). For each source Dn, $n = 0$–8, in the phantom, we constructed two binary masks. Circular mask $\boldsymbol{s}_n$ was constructed to select the exactly known pixels contained in Dn. Mask $\boldsymbol{b}_n$, for selecting surrounding background pixels, was obtained by subtracting $\boldsymbol{s}_n$ from a 6.2 cm diameter binary mask centered at Dn. Using these masks, we calculated S_n and B_n, the average intensities of the source and its surrounding background, by $S_n = \text{sum}(\boldsymbol{s}_n \boldsymbol{f})/\text{sum}(\boldsymbol{s}_n)$ and $B_n = \text{sum}(\boldsymbol{b}_n \boldsymbol{f})/\text{sum}(\boldsymbol{b}_n)$, respectively. The contrast of Dn was given by $C_n = S_n/B_n - 1$. Let C_n^{true} be the contrast of Dn obtained by applying the same calculations to Phantom 1. Then, the CRC for Dn was calculated by

$$\text{CRC}_n = C_n / C_n^{true} \tag{3}$$

For computing BV, following the NEMA procedure (National Electrical Manufacturers Association 2007) we defined 60 circular masks $\boldsymbol{b'}_m$ that equal $\boldsymbol{s}_n$ in size and placed these masks over the background region of the phantom without overlap. Let $\boldsymbol{b'} = \sum_m \boldsymbol{b'}_m$ be the union of these masks, we computed the mean and variance of the background by $B = \text{sum}(\boldsymbol{b'f})/\text{sum}(\boldsymbol{b'})$ and $\sigma^2 = \text{sum}((\boldsymbol{b'f} - B)^2)/\text{sum}(\boldsymbol{b'})$, respectively. The BV of the image was then given by

$$\text{BV} = \sigma / B \tag{4}$$

For each configuration and data noise level, five simulation runs were conducted, and the CRC and BV values obtained from these runs were averaged. To facilitate comparison, all CRC-versus-BV curves were plotted over the same CRC and BV ranges.

3. Experiments and results

3.1. Configuration with evenly distributed detector modules (M1)

The M1 configuration has evenly interleaved MTR and HTR detectors. We considered three sub-configurations that were obtained by employing 24, 16, or 12 HTR detectors (representing 1/2, 1/3, and 1/4 of the total number of detector modules) and identified them as M1–1/2, M1–1/3, M1–1/4, respectively. All detectors were first assumed to have the same DE so that $\alpha_i = 1$ for all LORs. Two noise levels were simulated for Phantom 1, corresponding to 300K and 1,000K total counts (1K = one thousand). Figure 4 shows the CRC-versus-BV curves obtained for all sources of the phantom for the M1–1/4 configuration from the 1,000K data as the number of iterations varies. There are no significant differences between the curves, which is also true for other symmetrical configurations (not shown). Therefore, below for S and M1 configurations we present only the curve averaged over all the sources.

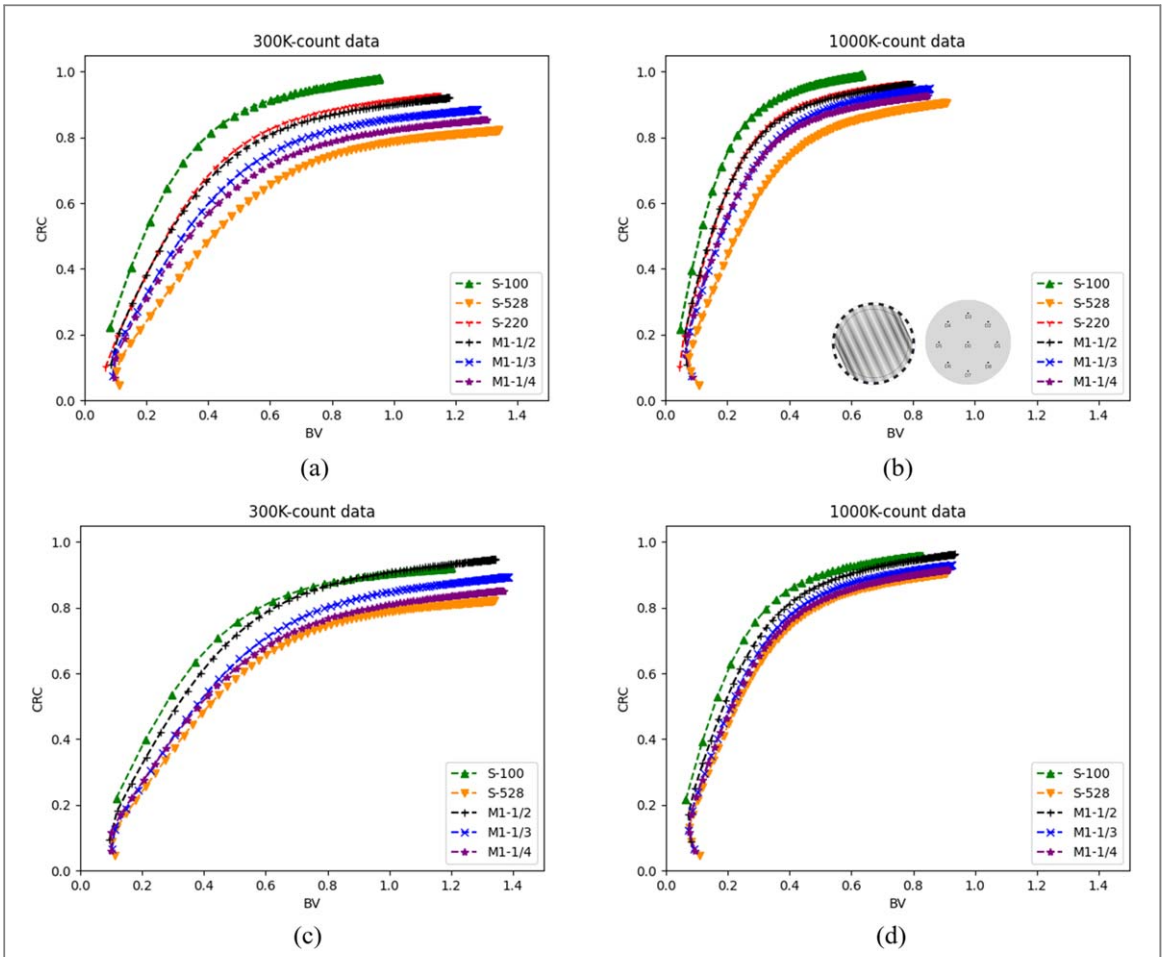

Figure 5. The average CRC-versus-BV curves of Phantom 1 obtained for M1, S-100, and S-528 configurations for 300K (a), (c), and 1,000K (b), (d). In (a) and (b), the MTR and HTR have the same DE, and the curve of M1–1/2 is empirically found to be similar to that of S-220. In (c) and (d), DEs are scaled according to the detector thickness, and same-duration data (see text) are considered. The insert in (b) shows Phantom 1 (35 cm diameter) and the M1 configuration of the scanner (78 cm diameter). For visuality, they are not shown at the same scale.

Figure 5(a) shows the resulting average CRC-versus-BV curves for various S and M1 configurations from the 300K data. As expected, at the same BV the S-100 curve has the highest CRC and the S-528 curve the lowest. Also, the CRC of the M1 configuration decreases as the number of HTR detectors decreases. At the same BV, the CRC of M1–1/2 is slightly higher than the average of the CRCs of S-100 and S-528. Interestingly, it is empirically found to be very similar to the CRC-versus-BV curve obtained by S-220. Figure 5(b) shows the CRC-versus-BV curves for the 1,000K data. The observations made above with the 300K data remain applicable but the vertical gaps between the curves are smaller. Comparing the curves in figures 5(a) and (b) for the same configuration, we observe that the latter has a small BV range, has a smaller BV and larger CRC at the same iteration number, generally has a large CRC at the same BV, and appears to converge toward a larger CRC. The first two observations can be attributed to the faster convergence rate when reconstructing higher-count data. The other two observations are consistent with that quantitatively more accurate images can be obtained from higher-count data. Disregarding S-220, curves in figure 5(a) (or figure 5(b)) similarly suggest that, when working with data having the same number of events, a faster convergence rate is achieved with configurations that employ more HTR detectors.

As discussed above, 100 ps CTR was often achieved by using crystals that are shorter than 10 mm and most current clinical systems employ 20 mm thickness crystals. In the second experiment, we accordingly assumed that the HTR and MTR detectors have 10 mm and 20 mm thickness, respectively. Based on these thicknesses and the attenuation coefficient of L(Y)SO for 511 keV gamma rays, we estimated that the DE of the HTR detector is 0.7 times that of the MTR detector. Hence, the type-M, type-H, and type-HM LORs will be assigned with α_i equal to 1.0, 0.49, and 0.7, respectively. Again, data containing 300K and 1,000K events were generated for S-528. For other configurations, data for the same durations were simulated; however, despite having fewer events they are still identified as 300K and 1,000K data. For distinction, we will refer to the previous experiments as 'same-count' and the current ones as 'same-duration'. Figures 5(c) and (d) plot the

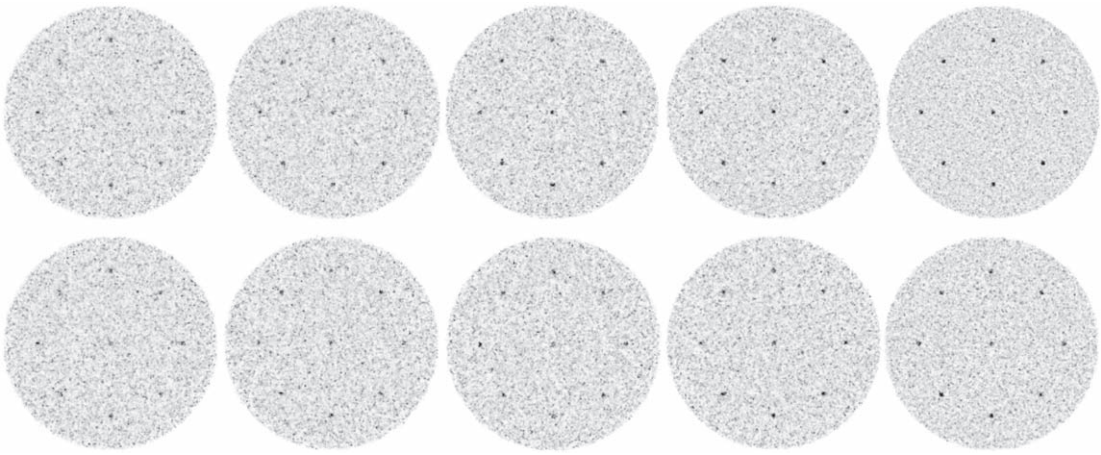

Figure 6. From left to right are images obtained for Phantom 1 with the S-528, M1–1/4, M1–1/3, M1–1/2, and S-100 configurations, from the 300K data in the same-count (top row) and same-duration experiments (bottom row). For these images, BV $\approx$ 0.5. The images are displayed using the same gray-level scale.

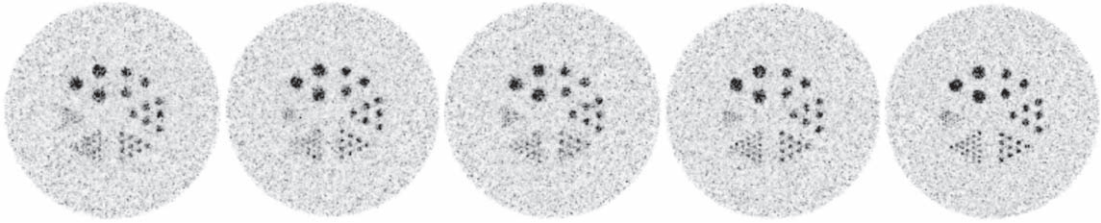

Figure 7. From left to right are images (BV $\approx$ 0.5) obtained for Phantom 2 with the S-528, M1–1/4, M1–1/3, M1–1/2, and S-100 configurations, from the 300K data in the same-duration experiment. The images are displayed using the same gray-level scale.

average CRC-versus-BV curves obtained for the 300K and 1,000K data, respectively. Comparing figure 5(c) with figure 5(a) (or figure 5(d) with figure 5(b)) shows that, except for S-528, at the same iteration number the CRCs (BVs) of all configurations have decreased (increased). At the same BV, S-100, and M1 now offer considerably less improvement in CRC over S-528. Moreover, after a sufficient number of iterations the M1–1/2 curve can reach higher CRCs at the same BV than does the S-100 curve. This suggests that, compared to the latter, the former has a slower convergence rate (due to a larger effective CTR of about 220 ps as demonstrated in figures 5(a) and (b)) but at convergence it can yield quantitatively more accurate images. Hence, as stipulated above, the benefit offered by the higher CTR of the HTR detector is now diminished due to its lower DE.

Figure 6 shows sample images obtained for Phantom 1 from the 300K data. To reduce the dependence on the number of iterations used, these images have approximately the same BV of 0.5. Also, the images were displayed by using the same gray-level scale. Subjectively, in agreement with the above observations, in both the same-count and same-duration experiments the S-100 image has the best quality (best visibility of the sources) and the S-528 image the worst (worse visibility of the sources). By comparing the bottom-row images to the top-row images, we observe increased image noise when the lower DE of the HTR detector is accounted for. This is most evident with S-100 because its DE is diminished the most.

Figure 7 shows sample images obtained for Phantom 2 from the 300K data in the same-duration experiment. Again, the BV values of these images are approximately 0.5. Subjectively, the 2 mm sources (smallest sources) cannot be resolved with all configurations. The 4 mm sources (second smallest sources) are readily visible in the M1–1/2 and S-100 images and are border-line visible in the M-528 image. Overall, the S-100 image is the best, and the S-528 image is the worst. The quality of the M1 images is superior to that of the S-528 image, with the M1–1/2 image comparing favorably with the S-100 image.

Below, we will consider the same-duration experiment that more realistically considers the lower DE of the HTR detector. In this case, type-H LORs have the lowest detection sensitivity and type-M LORs have the highest. When comparing two CRC-versus-BV curves, we examine their CRC values at the same BVs, and a curve is said to be *above* (*below*) another, and *better than (worse than*) another if its CRC values are greater (smaller). Also, the *gap* between the two curves refers to the difference in their CRC values at the same BV. When the gap between two curves is small, they are said to be *comparable* or *similar*.

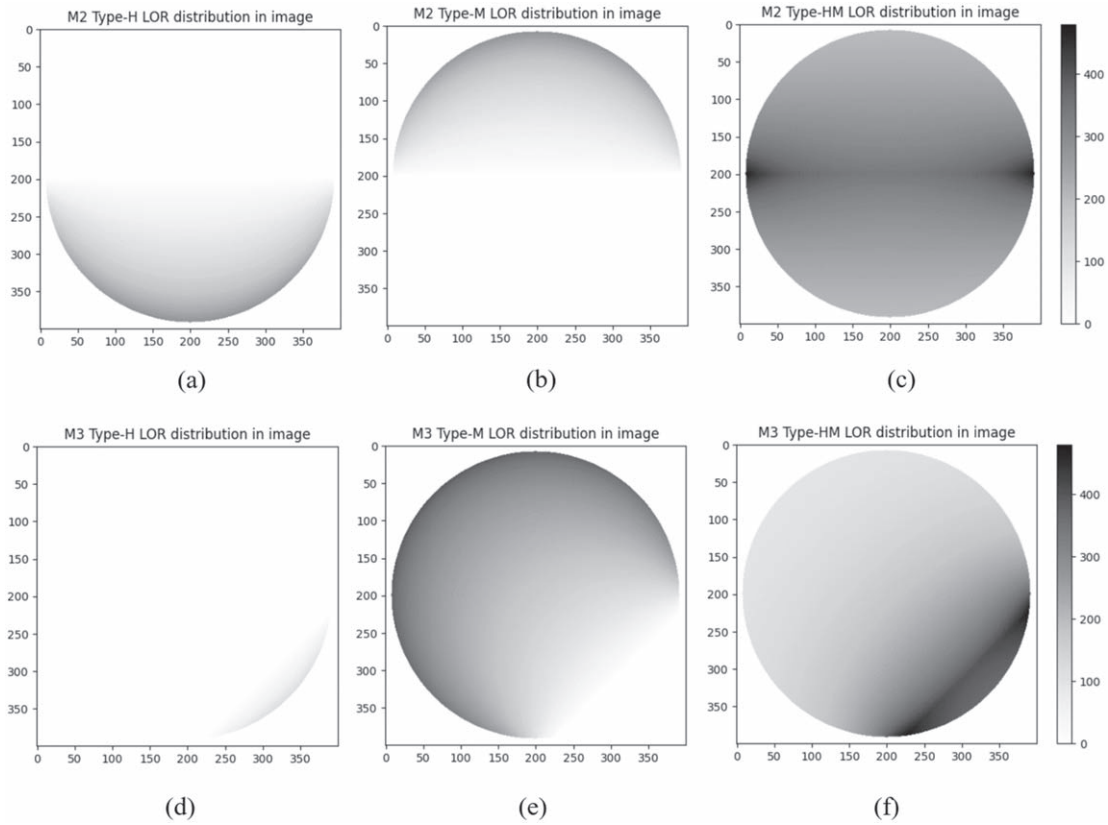

Figure 8. Density maps of type-H (a), Type-M (b), and type-HM (c) LORs passing through each image pixel for the M2 (top row) and M3 (bottom row) configurations.

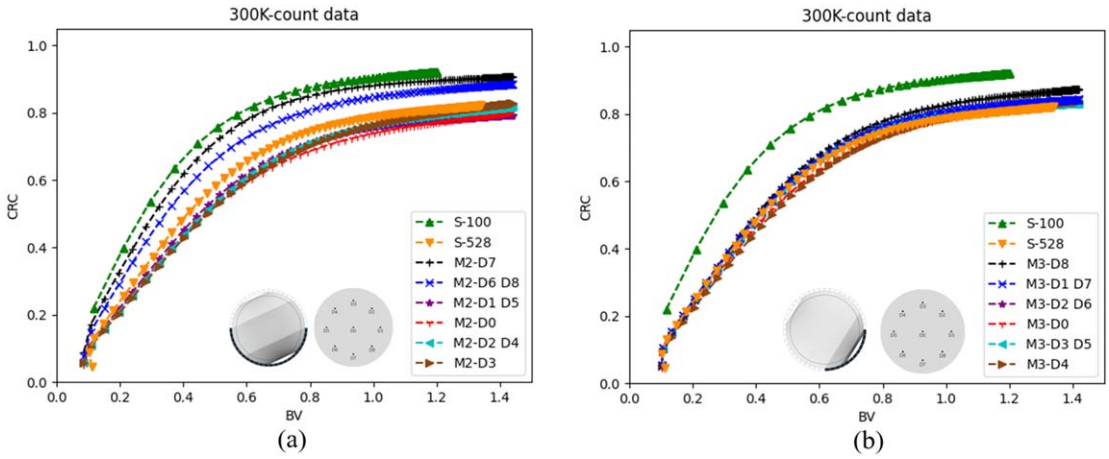

Figure 9. The CRC-versus-BV curves obtained for M2 (a) and M3 (b), in comparison with S-100 and S-528, from 300K-counts data in the same-duration experiment. The insert shows Phantom 1 (35 cm diameter) and the configurations of the scanner (78 cm diameter). For visuality, they are not shown at the same scale.

3.2. Configurations using two arcs of two detector types (M2 and M3)

As the M2 and M3 configurations have asymmetrical distributions of the two detector types, we expect them to yield nonuniform image properties. This is illustrated in figure 8 which shows the density maps for the three LOR types passing through the image pixels for the M2 and M3 configurations. Take M2 as an example, pixels in the lower (upper) half of the FOV are sampled predominantly by type-H (type-M) LORs and type-HM LORs, and pixels in the middle are predominantly by type-HM LORs. Below in figures 9 and 11, Mx-Dn designates the CRC-versus-BV curve obtained for source Dn (n = 0–8) by the Mx (x = 2–5) configuration. Figure 9(a) compares the curves obtained by M2 with those obtained by S-100 and S-528 for Phantom 1, from the 300K data in the same-duration experiment. At the same BV, the M2-D6,

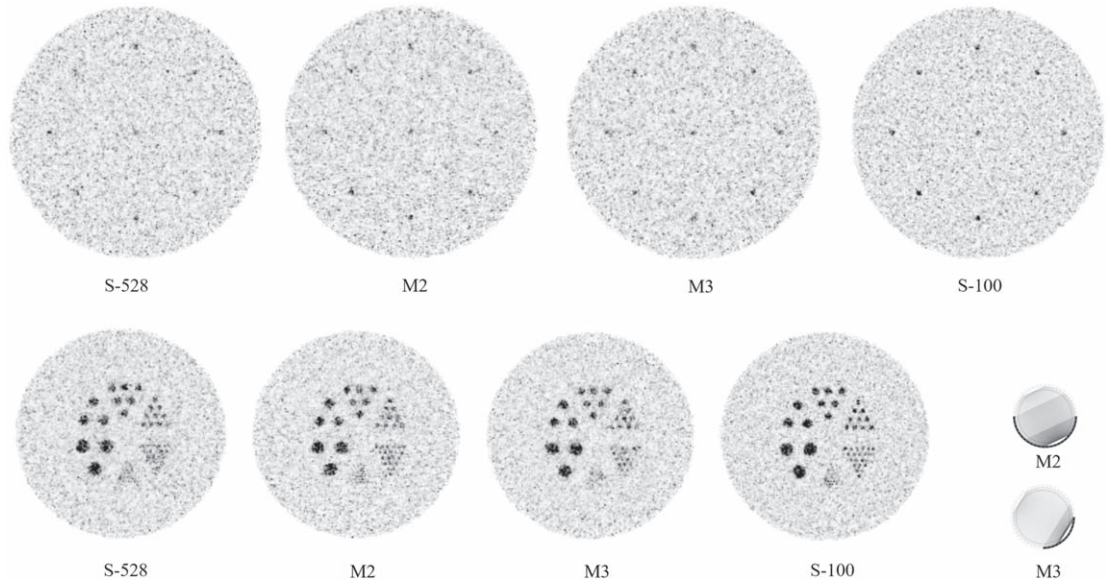

Figure 10. Top row: From left to right are images (BV ≈ 0.5) obtained for Phantom 1 (35 cm diameter) with S-528, M2, M3, and S-100 configurations, from 300K data in the same-duration experiment. The phantom is placed at the center of the scanner. Bottom row: Images with BV ≈ 0.5 obtained for Phantom 2 (30 cm diameter) that is placed at the center of the FOV for the S-518 and S-100 configurations, in the lower half for the M2 configuration, and the lower-right quadrant for the M3 configuration. The images are displayed using the same gray-level scale. The M2 and M3 configurations of the scanner (78 cm diameter) are also shown for reference. Note that the images and the scanner configurations are not displayed at the scale.

M2-D7, and M2-D8 curves have higher CRCs than the S-528 curve, with M2-D7 having the highest CRC, approaching that of S-100. This is consistent with the fact that these sources are in the lower half of the FOV that is preferentially sampled by type-H LORs (especially D7). After a sufficient number of iterations, curves obtained for other sources are comparable with the S-528 curve. These sources are in regions that are sampled by only type-M and type-HM LORs and where the lower DE of the HTR detector has offset the benefit offered by its better CTR. Figure 9(b) similarly shows the CRC-versus-BV curves obtained by M3 for Phantom 1, from the 300K data in the same-duration experiment. Compared to the M2 curves in figure9(a), as fewer HTR detectors are used the M3 curves are worse in general. Now, only the M3-D8 curve is above the S-528 curve; all other curves are similar.

Figure 10 shows the resulting images obtained for Phantoms 1 and 2, with the BV value equals to 0.5 approximately. The subjective quality of Phantom 1 images is consistent with the observations made above from the CRC-versus-BV curves: With respect to the S-528 image, visually the M2 image shows better quality in the lower FOV; elsewhere, it has comparable quality, but the center region is arguably inferior. The M3 image shows better (worse) quality in the lower-right (upper-left) quadrant of the FOV. Similarly, with Phantom 2 images we observe improved visibility for the 4 mm sources with M2 and M3 with respect to S-528 when they are placed in the favorable regions of these configurations.

The M1–1/2 and M2 configurations both employ 24 HTR detectors. Comparison of figures 9(a) and 5(c) shows that the best CRC-versus-BV curve (and most CRC-versus-BV curves) obtained with M2 is no better than (are inferior to) the average CRC-versus-BV curve obtained with M1–1/2. The M1–1/4 and M3 configurations both employ 12 HTR detectors. In this case, a comparison of figures 9(b) and 5(d) shows that the best CRC-versus-BV curve of M3 is better than the average CRC-versus-BV curve of M1–1/4. These observations suggest that the symmetric configurations are preferred when using relatively many HTR detectors but the asymmetric configurations may offer better image quality in specific regions when using relatively few HTR detectors. However, this observation is likely to be dependent on the detailed tradeoff characteristics between the improved CTR and diminished DE offered by the HTR detector.

3.3. Configurations with focus (M4 and M5)

We observed above that replacing MTR detectors with HTR detectors does not necessarily lead to improved image quality because the benefit offered by better CTR can be offset by diminished DE. Thus, if we are interested in improving the quality of a small region, it may be achieved by using a small number of HTR detectors to create type-H LORs for pixels in this region while maintaining the overall physical sensitivity of the system. For the purpose of demonstration, we examine an off-center focus region and a central focus region with the M4 and M5 configurations, respectively. We note that the D4 (D0) source of Phantom 1 is located inside the focus area of M4 (M5).

Figure 11(a) shows the CRC-versus-BV curves obtained by M4 from the 300K data in the same-

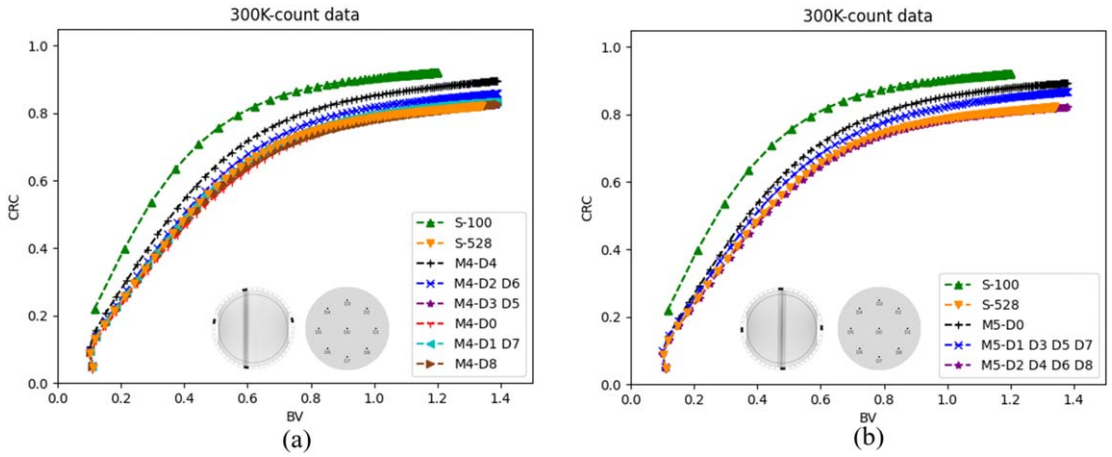

Figure 11. The CRC-versus-BV curves obtained for M4 (a) and M5 (b), in comparison with S-100 and S-528, from 300K data in the same-duration experiment. The insert shows Phantom 1 (35 cm diameter) and the configurations of the scanner (78 cm diameter). For visuality, they are not shown at the same scale.

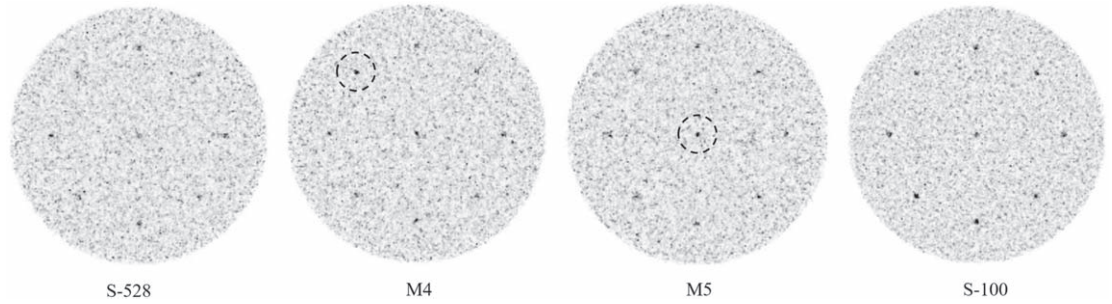

Figure 12. From left to right are images (BV $\approx$ 0.5) obtained for Phantom 1 (35 cm diameter) with S-528, M4, M5, and S-100 configurations, from 300K data in the same-duration experiment. The circles in the M4 and M5 images indicate the focus areas of these configurations. The images are displayed using the same gray-level scale.

duration experiment. For M4, the D4 curve is the best, which is consistent with the fact that D4 is in the focus area. With respect to the S-528 curve, the M4-D4 curve is noticeably higher and approaches the S-100 curve at large BV. In addition, it is slightly below the best M2 curves but is above the M3 curves shown in figure9. The D2 and D6 sources are seen by one pair of the HTR detector modules. Naturally, their curves are below M4-D4. However, they are still above S-528 and are slightly better or similar to the best M3 curve in figure9. For other sources, their curves are comparable with the S-528 curve. Therefore, based on the CRC-versus-BV evaluation the M4 configuration that employs only four HTR detector modules yields similar- or better-quality images than the M2 and M3 configurations that employ more than twelve HTR detector modules. Figure 11(b) shows the CRC-versus-BV curves obtained by M5. The observations made above with the M4 apply as well. Figure 12 compares the images obtained for Phantom 1 from the 300K data in the same-duration experiment by the M4, M5, S-528, and S-100 configurations. The results are consistent with the CRC-versus-BV assessment. Compared with S-528 (S-100), source visibility in the focus area of M4 and M5 is better (similar).

The above result indicates that it is feasible to use a small number of HTR detectors to boost the quality in a focus area without sacrificing quality in other regions. Therefore, we also aggressively consider using ultra-high time-resolution (UHTR) detectors that have a 10 ps CTR and the same DE as the HTR detector. Below, we will use M4–10 and M4–100 (M5–10 and M5–100) to designate the M4 (M5) configurations employing HTR and UHTR detectors respectively. Figure 13 compares the images obtained for Phantom 2 by S-100 and S-528 with those obtained by M4 and M5. In the latter cases, the phantom was positioned in such a way that the 4 mm sources group was inside their focus area. Again, the visibility of the 4 mm sources group in the M4–100 and M5–100 images is considerably superior to that of the S-528 image and slightly inferior to that of the S-100 image. In M4–10 and M5–10 images, the visibility of the 4 mm sources group is arguably better than that of the S-100 images.

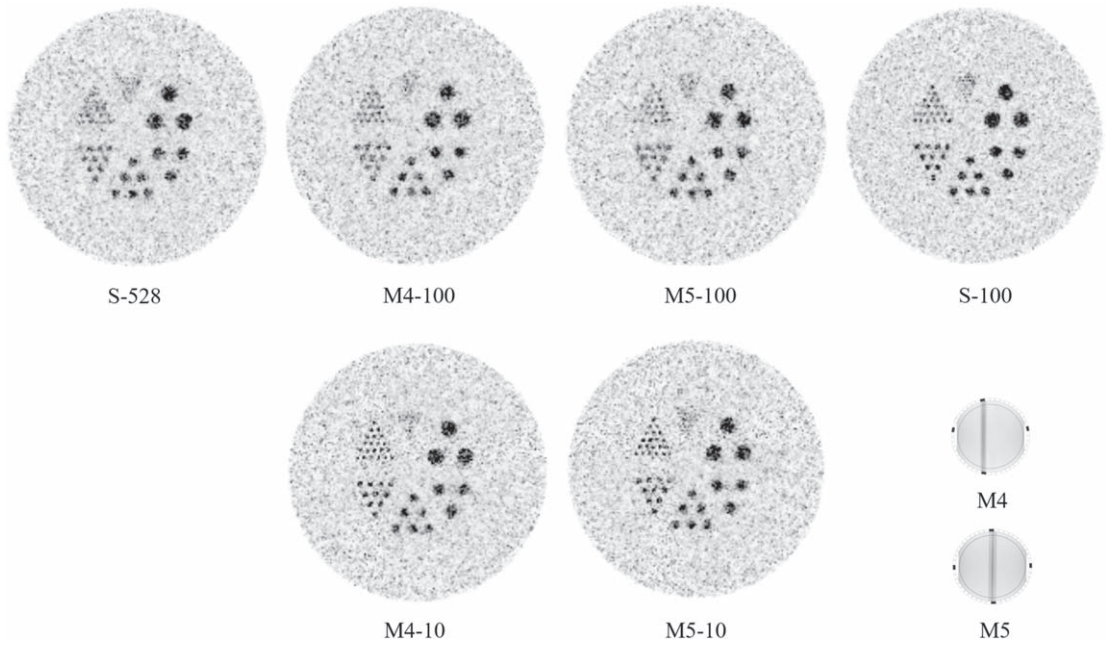

Figure 13. Reconstructed images obtained for Phantom 2 (30 cm diameter) from the 300K data in the same-duration experiment with S-528, S-100, M4, and M5 employing HTR detectors (M4–100 and M5–100), and M4 and M5 employing UHTR detectors (M4–10 and M5–10). For the S-100 and S-528 configurations, the phantom is placed at the center of the FOV. For the M4 and M5 configurations, the phantom is placed in positions where its 4 mm sources are in the focus regions of these configurations. The images are displayed using the same gray-level scale.

4. Conclusion and discussion

At present, due to technical challenges improving the CTR of a PET detector to 100 ps or better is likely to occur at the expense of its DE. As a result, employing such HTR detectors may not yield the image SNR gain as predicted by the conventional rule that does not factor into the diminished DE. With a significant reduction in the DE, it is even possible for the overall effective sensitivity of a system to decrease despite HTR detectors being used. It is also reasonable to expect HTR detectors to be much costlier and hence a PET system employing entirely HTR detectors may be prohibitively expensive. In this paper, we investigate employing two heterogeneous groups of HTR and MTR detectors for developing TOF PET systems. Specifically, we consider the HTR and MTR detectors to have 100 ps and 528 ps CTRs respectively, and the DE of the HTR detectors is 0.7 times that of the MTR detectors. Through computer simulation studies and considering 2d systems, we examine several representative ways of mixing the two detector groups, including symmetric configurations, asymmetric configurations, and configurations with a focus area. Our results indicate that a system that is fully populated with HTR detectors may not yield better image quality than one that is half populated with HTR detectors and half populated by MTR detectors. This reflects that the benefits of the better CTR of the HTR detector are offset by its diminished DE. Asymmetric configurations may be easier to implement but generally they yield nonuniform image quality. When using a relatively large number of HTR detectors, symmetric configurations seem to be better than asymmetric configurations. But when using a relatively small number of HTRs, asymmetric configurations may offer better image quality in some areas of the FOV. As an extreme case, we show that it is possible to improve the image quality in a focus area by using only four HTR detectors without noticeably compromising the quality in other areas of the FOV. However, asymmetric configurations and focused imaging may only be suitable for developing certain organ-specific systems (e.g. for cardiac imaging).

In conclusion, the results have shown the potential value of the proposed system-level design strategy of using heterogeneous detector groups for achieving high effective system sensitivity by factoring into the tradeoff between the CTR and DE of the detector. Only two detector groups are considered in this paper, but the idea can be generally applied to using more groups. This design strategy needs to be further validated by considering 3d imaging and including more physical factors that can be affected when increasing the CTR. For example, using thinner HTR detectors will reduce depth-of-interaction (DOI) blurring, will reduce random fraction (which is proportional to DE), and may increase scatter fraction (because the reduction in DE is larger for higher energy photons). How these factors affect the resulting image quality also strongly depends on the image reconstruction algorithm. In future work, we will conduct Monte-Carlo studies for more accurate 3d modeling and specifically consider optimization of the symmetric configuration by

considering the tradeoffs between imaging performance for whole-body cancer imaging applications and the fractional number of HTR detectors used. In actual implementation of this design strategy, it is desirable for the HTR and MTR detectors to be readily interchangeable. In reality, detectors in the same group do not have perfectly identical CTR. The effects of the CTR spread to the proposed design strategy need to be examined. For 3d systems, it is also possible to consider using interleaved MTR and HTR detector rings.

As already mentioned in section 1, HTR detectors with a high DE are possible by using side light readouts of thick scintillators. In addition, they provide DOI measurement and do not suffer from DOI blurring. For such HTR detectors, the tradeoff between CTR and DE is not strong. However, the proposed design strategy can still be useful for optimizing the imaging performance subject to certain cost constraints.

Acknowledgments

This work was supported in part by the National Natural Science Foundation of China under Grant No. 61927801 and 62250002, in part by The Mobility Programme of the Sino-German Center for Research Promotion under Grant No. M-0387, and in part by the start-up fund of the USTC 'Total solid angle PET-EPR multi-modality intelligent imaging'.

Data availability statement

All data that support the findings of this study are included within the article (and any supplementary files). Data will be available from 12 February 2027.

ORCID iDs

Zhiqiang Xin https://orcid.org/0000-0001-9842-9638
Chien-Min Kao https://orcid.org/0000-0002-8785-5225
Labao Zhang https://orcid.org/0000-0001-9205-7108

References

Badawi R D, Shi H, Hu P, Chen S, Xu T, Price P M and Cherry S R 2019 First human imaging studies with the EXPLORER total-body PET scanner *J. Nucl. Med.* **60** 299–303

Cates J W and Levin C S 2018 Evaluation of a clinical TOF-PET detector design that achieves ⩽ 100 ps coincidence time resolution *Phys. Med. Biol.* **63** 115011

Conti M 2011a Focus on time-of-flight PET: the benefits of improved time resolution *Eur. J. Nucl. Med. Mol. Imag.* **38** 1147–57

Conti M 2011b Improving time resolution in time-of-flight PET *Nucl. Instrum. Methods Phys. Res. A* **648** S194–8

Conti M and Bendriem B 2019 The new opportunities for high time resolution clinical TOF PET *Clinical and Translational Imaging Clin. Transl. Imaging.* **7** 139–47

Conti M, Bendriem B, Casey M, Chen M, Kehren F, Michel C and Panin V 2005 First experimental results of time-of-flight reconstruction on an LSO PET scanner *Phys. Med. Biol.* **50** 4507

Conti M, Eriksson L, Rothfuss H and Melcher C 2009 Comparison of fast scintillators with TOF PET potential *IEEE Trans. Nucl. Sci.* **56** 926–33

Gundacker S, Knapitsch A, Auffray E, Jarron P, Meyer T and Lecoq P 2014 Time resolution deterioration with increasing crystal length in a TOF-PET system *Nucl. Instrum. Methods Phys. Res.* A **737** 92–100

Hyman L G 1965 Time resolution of photomultiplier systems *Rev. Sci. Instr.* **36** 193–6

Jakoby B W, Bercier Y, Conti M, Casey M E, Bendriem B and Townsend D W 2011 Physical and clinical performance of the mCT time-of-flight PET/CT scanner *Phys. Med. Biol.* **56** 2375

Kwon S I *et al* 2021 Ultrafast timing enables reconstruction-free positron emission imaging *Nat. Photonics* **15** 914–8

Kyba C C, Glodo J, van Loef E V, Karp J S and Shah K S 2008 Energy and timing response of six prototype scintillators for TOF-PET *IEEE Trans. Nucl. Sci.* **55** 1404–8

Lecoq P 2017 Pushing the limits in time-of-flight PET imaging *IEEE Trans. Radiat. Plasma Med. Sci.* **1** 473–85

Lewellen T K 1998 Time-of-flight PET *Semin. Nucl. Med.* **28** 268–75

Liu J, Kao C M, Gu S, Xiao P and Xie Q 2014 A PET system design by using mixed detectors: resolution properties *Phys. Med. Biol.* **59** 3517

Miller M *et al* 2015 Characterization of the Vereos digital photon counting PET system *J. Nucl. Med.* **56** (**supplement 3**) 434–434

Moszynski M and Bengtson B 1979 Status of timing with plastic scintillation detectors *Nucl. Instr. and Meth.* **158** 1–31

National Electrical Manufacturers Association 2007 Performance measurements of positron emission tomographs *NEMA Standards Publication NU 2-2007* (Rosslyn, VA: National Electrical Manufacturers Association)

Nikolopoulos D *et al* 2006 Comparative study using Monte Carlo methods of the radiation detection efficiency of LSO, LuAP, GSO and YAP scintillators for use in positron emission imaging (PET) *Nucl. Instrum. Methods Phys. Res.* A **569** 350–4

Pan T *et al* 2019 Performance evaluation of the 5-ring GE discovery MI PET/CT system using the national electrical manufacturers association NU 2-2012 standard *Med. Phys.* **46** 3025–33

Pizzichemi M *et al* 2019 On light sharing TOF-PET modules with depth of interaction and 157 ps FWHM coincidence time resolution *Phys. Med. Biol.* **64** 155008

Pourashraf S, Gonzalez-Montoro A, Lee M S, Cates J W, Won J Y, Lee J S and Levin C S 2021a Investigation of electronic signal processing chains for a prototype TOF-PET system With 100-ps coincidence time resolution *IEEE. Trans. Radiat. Plasma Med. Sci.* **6** 690–6

Pourashraf S, Gonzalez-Montoro A, Won J Y, Lee M S, Cates J W, Zhao Z and Levin C S 2021b Scalable electronic readout design for a 100 ps coincidence time resolution TOF-PET system *Phys. Med. Biol.* **66** 085005

Rausch I, Cal-González J, Dapra D, Gallowitsch H J, Lind P, Beyer T and Minear G 2015 Performance evaluation of the Biograph mCT Flow PET/CT system according to the NEMA NU2-2012 standard *Eur. J. Nucl. Med. Mol. Imag. Phys.* **2** 1–17

Siddon R L 1985 Fast calculation of the exact radiological path for a three-dimensional CT array *Med. Phys.* **12** 252–5

Van Sluis J *et al* 2019 Performance characteristics of the digital Biograph Vision PET/CT system *J. Nucl. Med.* **60** 1031–6

Vandenberghe S, Moskal P and Karp J S 2020 State of the art in total body PET *Ejnmmi. Phys.* **7** 1–33